Theor. Comput. Fluid Dyn. (2012) 26:37–50
DOI 10.1007/s00162-010-0214-6

ORIGINAL ARTICLE

G. B. Jacobs · W. S. Don · T. Dittmann

High-order resolution Eulerian–Lagrangian simulations of particle dispersion in the accelerated flow behind a moving shock

Received: 2 February 2010 / Accepted: 8 October 2010 / Published online: 20 November 2010

Abstract This paper presents a computational study of the two-dimensional particle-laden flow developments of bronze particle clouds in the accelerated flow behind a moving normal shock. Particle clouds with a particle volume concentration of 4% are arranged initially in a rectangular, triangular and circular shape. Simulations are performed with a recently developed high-order resolution Eulerian–Lagrangian method that approximates the Euler equations governing the gas dynamics with the improved high order weighted essentially non-oscillatory (WENO-Z) scheme, while individual particles are traced in the Lagrangian frame using high-order time integration schemes. Reflected shocks form ahead of all the cloud shapes. The detached shock in front of the triangular cloud is weakest. At later times, the wake behind the cloud becomes unstable, and a two-dimensional vortex-dominated wake forms. Separated shear layers at the edges of the clouds pull particles initially out of the clouds that are consequently transported along the shear layers. Since flows separated trivially at sharp corners, particles are mostly transported out of the cloud into the flow at the sharp front corner of the rectangular cloud and at the trailing corner of the triangular cloud. Particles are transported smoothly out of the circular cloud, since it lacks sharp corners. At late times, the accelerated flow behind the running shock disperses the particles in cross-stream direction the most for the circular cloud, followed by the rectangular cloud and the triangular cloud.

Keywords Particles · Shock · Dispersion · High-Order · Eulerian-Lagrangian · WENO

1 Introduction

Shock waves are encountered in many technological environments, like supersonic aircraft, hypersonic space vehicles, jet engines and explosions. Often, the flow containing shocks interact with solid or liquid particles. For example, liquid or solid fuel particles interact with a chemically reacting fluid containing shock waves in high-speed combustors. Debris and dust particles interact with shocks and fluid turbulence in dust explosions. The particle dynamics and density distributions are of vital importance to the efficiency of combustors performances and the impact that particles have on the environment.

The analysis of particle-laden high-speed flow is challenging. At high-speeds, experimental investigations of the fluid mechanics are already extremely challenging, let alone the transport of high-velocity particles and their dynamics. The direct computational analysis of the particle-laden shocked flow requires the computation

Communicated by Hussaini.

G. B. Jacobs (✉) · T. Dittmann
Department of Aerospace Engineering & Engineering Mechanics, San Diego State University, San Diego, CA 92182, USA
E-mail: gjacobs@mail.sdsu.edu

W. S. Don
Department of Mathematics, Hong Kong Baptist University, Hong Kong, China
E-mail: wsdon@math.hkbu.edu.hk

of the complete flow over each particle, the tracking of individual solid or liquid complex particle boundaries along their paths, and the tracking of shock waves in the moving framework. The individual computational components are difficult to resolve and currently barely within reach even with the advances of computational technologies. The combined problem of shock and particles has an immense complexity, scale range and size, which can currently potentially be analyzed in highly idealized situation with a few particles.

Simplified models are required to handle more realistic situations. Eulerian-Lagrangian (EL) methods have provided outcome for particle-laden flows. In particular, EL methods that model particles as points like the particle-source-in-cell (PSIC) method [6]. In PSIC, the carrier gas is solved in the Eulerian frame on a mesh, while individual particles are modeled as points and are traced along their path in a Lagrangian formulation. The carrier gas and the particles are coupled through interpolation. The point modeling of particles enables the computation of a large, realistic number of particles and simulation of particle-laden flow in engineering applications, but the point model also inherently limits the type of flows that can be investigated to a dilute particle concentration.

The EL method typically relies on relatively simple, coarse grids and/or numerical schemes with low order of accuracy, i.e. first-order or second-order methods. Lower-order-based methods limit the accurate computation of particle-laden flows with a large range of active temporal and spatial scales. Dispersion and diffusion errors plague the accuracy of the solution. Shock-capturing schemes typically suffer even more from these errors, since the excessive diffusion that is needed to stabilize the methods near the shock dissipates important smaller-scale flow structures in the wake of the shock that governs the particle dynamics. In the EL approach, interpolation errors and high noise levels in the representation of particle influence on the flow can, moreover, contribute to numerical errors well in excess of model errors leading to misrepresentation of the true particle-laden flow physics.

For problems in which a large number of scales coexist, high-order and high-resolution numerical algorithms have great potential to accurately and efficiently capture all flow features for long time. In [7], we initiated the development of a high-order PSIC algorithm for the computation of particle-laden flow with shocks. We solved the gas dynamics with an improved high-order weighted essentially non-oscillatory schemes (WENO-Z) [2]. WENO-Z scheme is an improved version of the classical WENO-JS scheme as designed by Jiang and Shu [9]. The WENO-Z scheme uses a global higher order smoothness indicator formed by a linear combination of lower order local smoothness indicators to form new WENO nonlinear weights. The new WENO-Z nonlinear weights satisfy the necessary and sufficient condition to guarantee the formal order of accuracy of the WENO-Z scheme, which the classical WENO-JS scheme has failed to achieve for smooth functions. Numerical experiments also demonstrate that the WENO-Z scheme has higher resolution than the WENO-JS scheme in shocked flows. The WENO-Z based PSIC method proven very effective for the simulation of the fine scale and delicate structures of the physical phenomena involving shocks [5,11,12]. A consistent and stable high-order ENO interpolation was introduced for interpolation of the gas flow to the particle. A smooth higher-order weighting ensured a low noise and accurate coupling of the particles to the gas. Time integration of the carrier phase and the particles is performed with a high-order Runge–Kutta TVD method without splitting.

In this paper, we initiate our effort towards a thorough validation of the EL method and assessment of numerical and model errors. We aim to validate our high-order resolution EL against experiments in Boiko et al. [3] and Kiselev et al. [10] on the dispersion of cloud of particles in the accelerated wake behind a moving shock. Boiko et al. analyzed the interaction between an initially rectangular cloud shape of particles with the accelerated flow behind a running shock experimentally in a shock tube. In Boiko et al. [3], these experiments were partially validated. Later, Kiselev et al. [10] reported on the same results but with improved grid resolution.

We focus on the effect of the initial shape of the particle cloud on the dispersion patterns at later times. We consider an initially rectangular, triangular and circular shape of bronze particles with dilute particle volume concentrations. The findings set the stage for a detailed ongoing comparison of the computationally and experimentally determined dispersion patterns. We show that the change of initial shape dramatically changes shock patterns and shear flows that affect the particle dispersion and concentration at early and late times. Detonation type shock waves will have the largest impact on particle dispersion in the circular cloud shape, while the particles in the triangular cloud shape disperse the least in the accelerated flow behind a moving shock.

We will briefly review the developed high-order resolution EL method followed by a discussion of a moving shock interacting with a cloud of particles that have three different initial shapes including a rectangle, a triangle and a circle. In Sect. 2, the PSIC formulation is presented. We give a brief description of the improved fifth-order weighted essentially non-oscillatory WENO-Z scheme. We summarize the high-order particle algorithm,

including interpolation, weighing and time integration. In Sect. 3, we discuss the two-dimensional shock-particles cloud interactions computed with the high-order PSIC method. In Sect. 4, the effect of initial shape of particle clouds (rectangular, triangular and circular shapes) on the dispersion patterns of the particles and the evolution of the flow fields will be presented and discussed. Conclusion and direction of future research are given in Sect. 5.

2 The physical model and particle-source-in-cell method

In the particle-source-in-cell (PSIC) method, the Eulerian continuum equations are solved for the carrier flow in the Eulerian frame, while particles are traced along in the Lagrangian frame.

In the following, we shall denote the subscript p for the particle variables and f for the gas variables at the particle position. Variables without subscript refer to the gas variables unless specified otherwise.

2.1 Euler equations in the Eulerian frame

The high-speed flows that we are considering have very high Reynolds numbers and are thus convection dominated flows. We, therefore, do not model viscous effects in the governing Eulerian equations for the gas flow (1). The governing equations for the carrier flow are the two-dimensional Euler equations in Cartesian coordinates given by:

$$\mathbf{Q}_t + \mathbf{F}_x + \mathbf{G}_y = \mathbf{S}, \tag{1}$$

where

$$\begin{aligned} \mathbf{Q} &= (\rho, \rho u, \rho v, E)^T, \\ \mathbf{F} &= \left(\rho u, \rho u^2 + P, \rho uv, (E + P)u\right)^T, \\ \mathbf{G} &= \left(\rho v, \rho uv, \rho v^2 + P, (E + P)v\right)^T, \end{aligned} \tag{2}$$

and the equation of state is

$$P = (\gamma - 1)\left(E - \frac{1}{2}\rho\left(u^2 + v^2\right)\right), \qquad \gamma = 1.4 \tag{3}$$

$$T = \frac{\gamma P M^2}{\rho}, \tag{4}$$

where $M = U/\sqrt{\gamma RT}$ is a reference Mach number determined with the reference velocity, U, and reference temperature, T. The source term, $\mathbf{S}$, accounts for the effect of the particles on the carrier gas and will be discussed in more detail below.

2.2 Particle equation in the Lagrangian frame

Particles are tracked individually in the Lagrangian frame. The kinematic equation describing the particle's position, $\mathbf{x}_p$, is given as

$$\frac{\mathrm{d}\mathbf{x}_\mathrm{p}}{\mathrm{d}t} = \mathbf{v}_p, \tag{5}$$

where $\mathbf{v}_p$ is the particle velocity vector.

The particles' acceleration is governed by Newton's second law forced by the drag on the particle. With particles assumed spherical, we take the drag as a combination of the Stokes drag corrected for high Reynolds and Mach number and the pressure drag leading to the following equations governing the particle velocity [3],

$$\frac{\mathrm{d}\mathbf{v}_\mathrm{p}}{\mathrm{d}t} = f_1\left(\frac{\mathbf{v}_f - \mathbf{v}_p}{\tau_p}\right) - \frac{1}{\rho_p}\nabla P|_f, \tag{6}$$

where $\mathbf{v}_f$ is the velocity of the gas at the particle position, ρ_p the particle density. The first term on the right-hand side describes the particle acceleration resulting from the velocity difference between the particle and the gas. f_1 is an empirical correction factor [3] that yields an accurate determination within 10% of measured particle acceleration for higher relative particle Reynolds number up to $Re_p = p_f\, d_p|v_f|\; Re_p$ = 10,000 and relative particle Mach number up to $M_f = |\mathbf{v}_f|/\sqrt{T_f} = 1.2$ and is given by

$$f_1 = \left(18 + 0.285 Re_p + 3\sqrt{Re_p}\right)\left(1 + \exp\left[\frac{-0.43}{M_f^{4.67}}\right]\right). \tag{7}$$

The second term is the particle acceleration induced by the pressure gradient in the carrier flow at the particle position. The particle time constant $\tau_p = Re d_p^2 \rho_p/18$, where d_p is the particle diameter, is a measure for the reaction time of the particle to the changes in the carrier gas. $Re_f = UL/\nu$ is the Reynolds number of the carrier gas flow with L a reference length and ν the dynamic viscosity.

The particle temperature is mostly affected by convection. From the first law of thermodynamics and Fourier's law for heat transfer, the equation for temperature is derived as,

$$\frac{dT_p}{dt} = \frac{1}{3}\frac{Nu}{Pr}\left(\frac{T_f - T_p}{\tau_p}\right), \tag{8}$$

where $Pr = 1.4$ is the Prandtl number, taken as its typical value for air in this paper. $Nu = 2 + \sqrt{Re_p} Pr^{0.33}$ is the Nusselt number corrected for high Reynolds number.

2.3 Source term **S** for the Euler equation

Each particle generates a momentum and energy that affects the carrier flow. The volume-averaged summation of all these contributions gives a continuum source contribution on the momentum and energy equation in (1) as:

$$\mathbf{S}_m(\mathbf{x}) = \sum_{i=1}^{N_p} \mathbf{K}_i(\mathbf{x}_p, \mathbf{x})\mathbf{W}_{m,i}, \tag{9}$$

$$S_e(\mathbf{x}) = \sum_{i=1}^{N_p} \mathbf{K}_i(\mathbf{x}_p, \mathbf{x})(\mathbf{W}_{m,i} \cdot \mathbf{v}_p + W_{e,i}), \tag{10}$$

where $\mathbf{K}_i(x_i, y) = \mathbf{K}(|x_i - y|)/V$ is a normalized weighting function that distributes the influence of each particle onto the carrier flow. $\mathbf{W}_{m,i} = [m_p f_1(\mathbf{v}_f - \mathbf{v}_p)/\tau_p]_i$ and $W_{e,i} = [m_p(Nu/3Pr)\left(T - T_p\right)/\tau_p]_i$ are weight functions describing the momentum and energy contribution of one particle, respectively. m_p is the mass of one spherical particle that can be derived from τ_p. N_p is the total number of particles in a finite volume V. The normalized weighting function will be further discussed below.

2.4 Flow solver

The carrier flow Eq. 1 are discretized spatially with a fifth-order weighted essentially non-oscillatory conservative finite difference scheme (WENO-Z) [4] on a uniform mesh and temporally with the third-order Runge–Kutta TVD scheme.

The nonlinear nature of the hyperbolic Euler equations admits finite time singularities in the solution even when the initial condition is smooth. It is important that the numerical methods employed avoid non-physical oscillations, also known as the Gibbs phenomenon, when the solution becomes discontinuous. Among many high-order shock-capturing schemes, the weighted essentially non-oscillatory finite difference schemes (WENO) for conservation laws [9] has been very successfully employed for the simulation of the fine scale and delicate structures of the physical phenomena related to shock-turbulence interactions.

The essence of the WENO scheme is the nonlinear adaptive stencils, where a nonlinear convex combination of lower-order polynomials adapts either to a higher-order central upwinding approximation at smooth parts of the solution, or to an upwind lower-order spatial discretization that avoids interpolation across discontinuities

and provides the necessary dissipation for shock capturing. The nonlinear coefficients of the convex combination, hereafter referred to as classical weights, are based on the local smoothness indicators, which measure the sum of the normalized squares of the scaled L^2 norms of all derivatives of the lower-order polynomials. An essentially zero weight is assigned to those lower-order polynomials whose underlining stencils contain high gradients and/or shocks, yielding an essentially non-oscillatory solution at discontinuities. At smooth regions, higher order is achieved through the mimicking of the central upwinding scheme of maximum order, when all the smoothness indicators are about the same size. The classical weights were later further improved by Borges et al. that made use of existing higher-order information contained within the stencils. The improved weights [4] (WENO-Z) were shown to satisfy the necessary and sufficient conditions for the optimal order of the given fifth-order scheme.

At each grid point, the first-order Lax-Friedrichs flux splitting is used as the low-order building block to split the Euler flux, ignoring the source term, into the positive and negative going fluxes. The positive and negative going fluxes are then decomposed into the characteristic variables via the left eigenvectors and eigenvalues of the Euler flux. The eigensystem of the Euler flux is obtained via the linearized Riemann solver of Roe [13]. The characteristic variables are then reconstructed via the improved high-order weighted essentially non-oscillatory (WENO-Z) scheme as discussed above. The reconstructed characteristic variables are then re-projected back into the physical space as the numerical flux via the right eigenvectors (see Shu et al. [9] for further details.)

2.5 Particle solver

Lagrangian tracking of the particles consists of three stages per particle, including searching the element a particle is located in, interpolating the field variables to the particle location and moving the particle forward with a time integration method.

Locating the host cell of a particle is a trivial task on a structured grid. Following Jacobs and Hesthaven [8], to avoid aliasing errors and an unphysical numerical total energy increase, the order of interpolation has to equal the approximation order k of the stencil S_k and the time integration of the particle solver and the carrier phase solver have to match. To determine the field variables at the particle location, we use the ENO interpolation introduced by Jacobs and Don [7] suited to flows containing shock discontinuities. The ENO interpolation was shown to prevent Gibbs oscillations that plague the accuracy of the centered interpolation over shocks.

In smooth flow areas without shocks, the WENO-Z method uses a central difference scheme. A centered interpolation to the particle position is then most accurate and preferred. We use Lagrange interpolating polynomial of degree k,

$$\mathbf{P}_k(x_p) = \sum_{i=i_p-k/2}^{i_p+k/2} \mathbf{Q}(x_i) l_i(x_p), \tag{11}$$

where i_p represents the nearest cell center to the left of the particle position. The number of points k should be equal to the number of points used as the order of the WENO scheme [8]. In the case of the fifth order WENO scheme, $k = 5$.

In shocked regions, the centered interpolation will produce undesirable Gibbs oscillations. With an ENO interpolation [14], these oscillations are essentially removed. ENO interpolation is only necessary in WENO-domains identified by the smoothness indicator. In those domains, the interpolating points are determined based on smoothness of the function indicated by the divided differences. The k-th degree-divided differences are determined first.

The 0th-order divided differences of Q are defined by:

$$Q[x_i] \equiv Q(x_i). \tag{12}$$

The jth degree-divided difference for $j \geq 1$ are defined by

$$Q[x_i, \ldots, x_{i+j}] \equiv \frac{Q[x_{i+1}, \ldots, x_{i+j}] - Q[x_i, \ldots, x_{i+j-1}]}{x_{i+j} - x_i}. \tag{13}$$

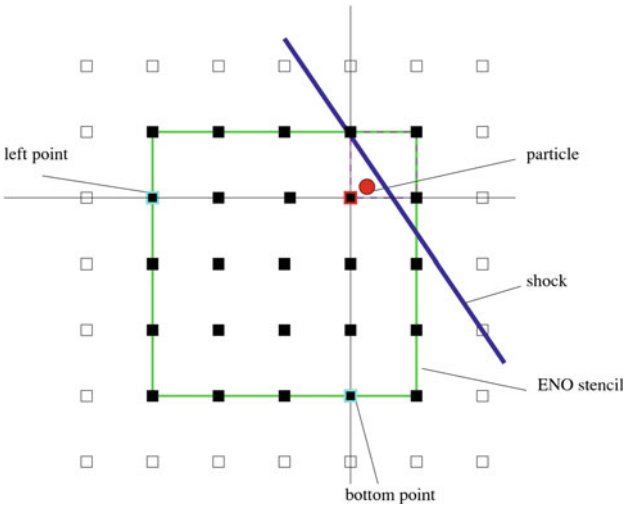

Fig. 1 Two-dimensional ENO stencil for interpolation to a particle located near to a shock. The *left* and *bottom* point of the interpolation stencil is determined based on the divided differences along the *horizontal grid lines* and *the vertical grid lines* at the particle's nearest grid point to the *left* and *bottom* of the particle

Starting from a two-point stencil, x_{i_p}, x_{i_p+1}, the interpolation stencil is expanded to k points based on a comparison of the divided differences of the increasing order at i_p. The smallest second order divided differences at i_p of the two potential three point stencils $\min\left\{Q[x_{i_p-1}, x_{i_p}, x_{i_p+1}], Q[x_{i_p}, x_{i_p+1}, x_{i_p+2}\right\}$ indicates the smoothest interpolation stencil and is therefore chosen. This procedure is repeated until a k point interpolant is found. The Lagrange interpolant in (11) then interpolates to the particle position.

In two dimensions, the same procedure can be used along the separate dimension on the tensor grid. The divided differences are determined along horizontal and vertical lines in the grid. With the 1D approach outline above, we find the left most and bottom most grid point of the interpolation stencil with $k \times k$ points for each grid point in the domain.

We give an example of a two-dimensional ENO stencil in Fig. 1. The particle's nearest grid point is found to the bottom, left of the particle. The left and bottom point of the ENO stencil is determined by comparison of the divided difference along the horizontal and vertical line crossing the nearest grid point. If a particle is located in a cell with a shock, then the ENO is one-sided to the left and bottom of the particle. We note that if two shocks cross the k interpolation stencil, then this procedure will fail to recognize the second shock. This is, however, mostly a rare short-lived event. We did not encounter stability problems in the simulations we performed below.

To determine the particle influence on the carrier flow (10), we use the high-order spline interpolation discussed in Ref. [1] and presented in Ref. [7]. The high-order weighing reduces aliasing and noise in the sources (10) that couple the particles to the gas flow. The spline S_k is constructed by the convolution of the square nearest-grid-point or zero order weighting function, where k is the degree of the spline interpolant. For $k = 0$ this yields a tophat function, which is often used in lower order PSIC methods. For large k the spline approaches the Gaussian function. In this case, the 0_th mode of function in wave space is free of aliasing errors, and the higher component of the function in wave space are smaller than equivalent Lagrangian interpolations.

3 Dispersion patterns of an initially rectangular cloud in accelerated flow behind a shock

In [7], we revisited the interaction of a moving shock with a cloud of bronze particles in 1D and 2D studied by Boiko et al. [3] and Kiselev et al. [10]. We demonstrated that the high-order resolution EL method improved the capturing of the small-scale flow structures behind the moving shock, while the global features compared well to the computations and experiments by Boiko and Kiselev. We also discussed the long-time particle dispersion of an initial rectangular cloud shape in the accelerated flow behind a shock. In this section, we will summarize the findings from [7], which sets the stage for a comparison with a initially circular and triangular cloud shape in the next section.

3.1 Initialization

The rectangular cloud is seeded with uniformly distributed particles at $[0.175, 0.352] \times [0.044, 0.044]$ with zero initial velocity. The volume concentration of the particles in all cloud shapes is 4% to ensure a relatively dilute particles concentration according to the model assumption. The particle response time and density are $\tau_p = 51.69$ and $\rho_p = 7.42 \times 10^4$, respectively, corresponding to an experiment with bronze particles in [10]. We take the Reynolds number needed to compute the particle traces according to the experiment at $Re_p = 3.387 \times 10^7$.

We initialize a right moving shock with $M_s = 3$ at $x_s = 0.175$ in a rectangular domain $[0, 3] \times [-0.611, 0.611]$. The state of the pre-shock flow is $[\rho_R, u_R, p_R] = [1, 0, 1]$. The post-shock state can be computed via the well-known Rankine–Hugoniot relations for a given Mach number M_s. Free stream inflow and outflow boundary conditions are imposed in the inflow and outflow boundaries, respectively, in the x direction. A periodical boundary condition is imposed in the y direction. The cloud is seeded directly before the shock at time, $t = 0$.

The number of grid points used to find the flow solution in the Eulerian frame is $1,500 \times 500$ in the x and y directions, respectively. The total number of particles is 40 K. Each computational particle represents 3,600 real bronze particles.

3.2 Particle-laden flow patterns

In Fig. 2, we present snapshots of the vorticity magnitude $|\omega|$ (left column) and the trajectory of the particles (right column) at non-dimensional times $t = 0, 0.05, 0.1, 0.225, 0.5, 0.75$. The dotted rectangle in the figures shows the original shape and position of the particles at $t = 0$ for reference.

In the time interval from $t = 0$ to $t = 0.05$, the right moving Mach 3 shock hits the particle and a reflected bow shock forms at the front end of the *shape* as seen in the vorticity plot (Fig. 2, left column). The right-moving shocks move along the top and bottom sides of the *shape* and are curved close to the *shape*. Strong vorticity ω is generated by the accelerated flow in the wake of the curved shock. The shear layer emanating from the front corners of the *shape* is also clearly visible by the increased vorticity magnitude in Fig. 2 (left column). The accelerated flow stagnates at the front of the *shape* and compresses the *shape*. The particles at the front end move towards the right at this early time and increase the particle density (Fig. 2, right column).

At times $t = 0.1$ and $t = 0.225$, the main shock has moved past the *shape* and the two curved shocks originated from the top and bottom of the *shape* have moved towards and crossed the symmetry line at $y = 0$. A Mach reflection occurs once the curved shocks have crossed the symmetry lines, which connects the curved shock and the right-moving main shock. Further in time, the flow complexity significantly increases, when the non-linearly interacting curved shocks affect the compression wave in the particle cloud, and the vorticity generated at the rear end of the cloud.

The force exerted by the particles on the accelerated gas behind the main shock leads to a flow pattern comparable to a flow over a blunt body. The flow separates on the top and bottom sides of the *shape*, and a recirculation forms at the back of the *shape*. The *shape* is compressed inward on the top and bottom sides toward the symmetry line at $y = 0$ as shown in the trajectory of the particles. The strong vorticity in the separated shear zones pulls the particles out of the *shape*, which leads to the formation of the particle arms and legs on the side and the back of the *shape*. The arms and legs follow the separated shear layers. At the back of the shape, the particle legs thus bend inward and the particle arm on the sides moves upward and downstream.

The gas density increases inside the shape, but the pressure remains constant (not shown). The particles cool the gas through heat exchange [10]. The lowered temperature leads to an increased density to satisfy the ideal gas law, since the pressure remains constant in the cloud to balance the particle force. The overall flow field maintains its symmetry up to this point in time.

The flow becomes unstable and loses its symmetry at later time (See figures for $t = 0.5$ and $t = 0.75$). In the wake of the *shape*, an asymmetric shedding is observed in the vorticity contour (Fig. 2, left two column). Increasingly, more particles are dispersed upward and downstream of the cloud forming long and thicker particle arms into the main flow and around the shape. A compression wave that formed at the side of the *shape* at early time has now moved sideways away from the symmetry line and has run into the particle arms. This compression wave reshocks the particle-laden flow in the arms and further widens the particle arms. This re-shocking induces intermittent wave patterns in the side shear layer that interacts with the particles forming streaks and bunching of the particles.

Throughout the computed time interval, the side arms shield the high-speed flow generated by the right-moving shock from the wake of the *shape*. Only a small number of particles are dispersed in the legs at the rear of the *shape*, since the side arms divert the main high-speed flow away from the shape and the relatively low flow velocities in the wake of the *shape* do not carry the particles as much as in the side arm.

4 Effect of initial cloud shape on dispersion patterns

4.1 Initialization of particle clouds

To make a fair comparison between cases with different initial cloud shapes, we ensure that we initialize the particle clouds with the same volume concentration covering the same geometric area and at the same location. The circle is thus initialed with a radius of 0.0704 yielding the same surface area as the rectangle. The circle center is at (0.2454, 0). For the initial triangle to cover the same surface area as the rectangle and the circle, the height of the triangle has to be 0.176. The volume concentration of the particles in all cloud shapes is 4%. Further initialization is the same as discussed above for the initially rectangular cloud shape.

4.2 Particle-laden flow development at early time

We discuss the particle-laden flow development through snapshots of the vorticity and the particles at four non-dimensional times of $t = 0.1, 0.225, 0.5, 0.75$ in Figs. 2, 3 and 4. The vorticity magnitude $|\omega|$ is plotted in the left column and the trajectory of the particles in the right column. A dotted rectangle, circle and triangle in the figures show the original shape and position of the particles at $t = 0$ for reference.

The overall flow field maintains its symmetry at early times up to $t = 0.225$. At later times, the wake behind the cloud is unstable.

When the right-moving shocks hit the particle cloud, a reflected shock forms at the front end of the cloud for each cloud shape. This shock development as visualized by the vorticity magnitude generated by the shock is comparable for the rectangular and circular shape. In both cases, a strong detached "bow" curved shock forms with a large part of the shock normal to the flow, as typical for blunt objects. The bow shock moves upstream at comparable velocity from $t = 0.1$ to $t = 0.225$ for the rectangle and circle. At the sharp front corner of the triangle, the reflected shock, however, stays attached until $t = 0.1$ and does not move significantly upstream throughout the flow development.

The right-moving shock moves along the top and bottom sides of the clouds and has passed the cloud at time $t = 0.1$. The refracted shock is curved towards the symmetry line at $y = 0$. Since the triangle is wider at the back end and hence the distance to the symmetry line larger, the curvature of the right shock is larger for the triangle when compared to the other two cases.

At early times, the particle clouds act like solid bodies in gas flow. The interaction of the accelerated flow with the particle cloud leads to an increased vorticity near the cloud. At sharp edges, the flow separates from the cloud. The flow separates at the front corners of the rectangular cloud. The shear layer reattaches to the cloud further downstream and separates again at the trailing edge. In the triangular cloud shape cases, a shear layer separates only at the sharp trailing edge. The circle has no sharp edge, and the separation location moves forward from time $t = 0.1$ to $t = 0.225$ along the boundary of the circle.

The separated shear layer is strongly correlated to the transport of particles out of the cloud into the flow at early times. The strong vorticity in the separated shear zones pulls the particles out of the shape, hence, forming the distinct arms and legs observed in the previous section for the rectangle [7], and the two particle streaks at the rear of the triangular cloud shape. Since the shear layer moves for the circular cloud shape case, the particle streaks out of the shape are less sharp as for the other two cases.

The accelerated flow stagnates at the front of the blunt rectangular and circular cloud shapes and compresses these clouds. The particles at the front end move towards the right at this early time and increase the particle density. The sharp edge of triangle yields a much lesser compression, and the front location of the triangle has not moved towards the right as far as for the other two cases at $t = 0.225$. The sides of the triangle, however, are pushed more inward toward the symmetry line. The rectangular shape is also slightly compressed inward by the reattached flow on the top and bottom sides toward the symmetry line at $y = 0$.

In the wake of the shapes, initially, two typical recirculation zones form that stretch in flow direction from $t = 0.1$ to $t = 0.225$. The reduced pressure and negative flow velocity push the rear edge of the particle cloud perhaps counter intuitively upstream.

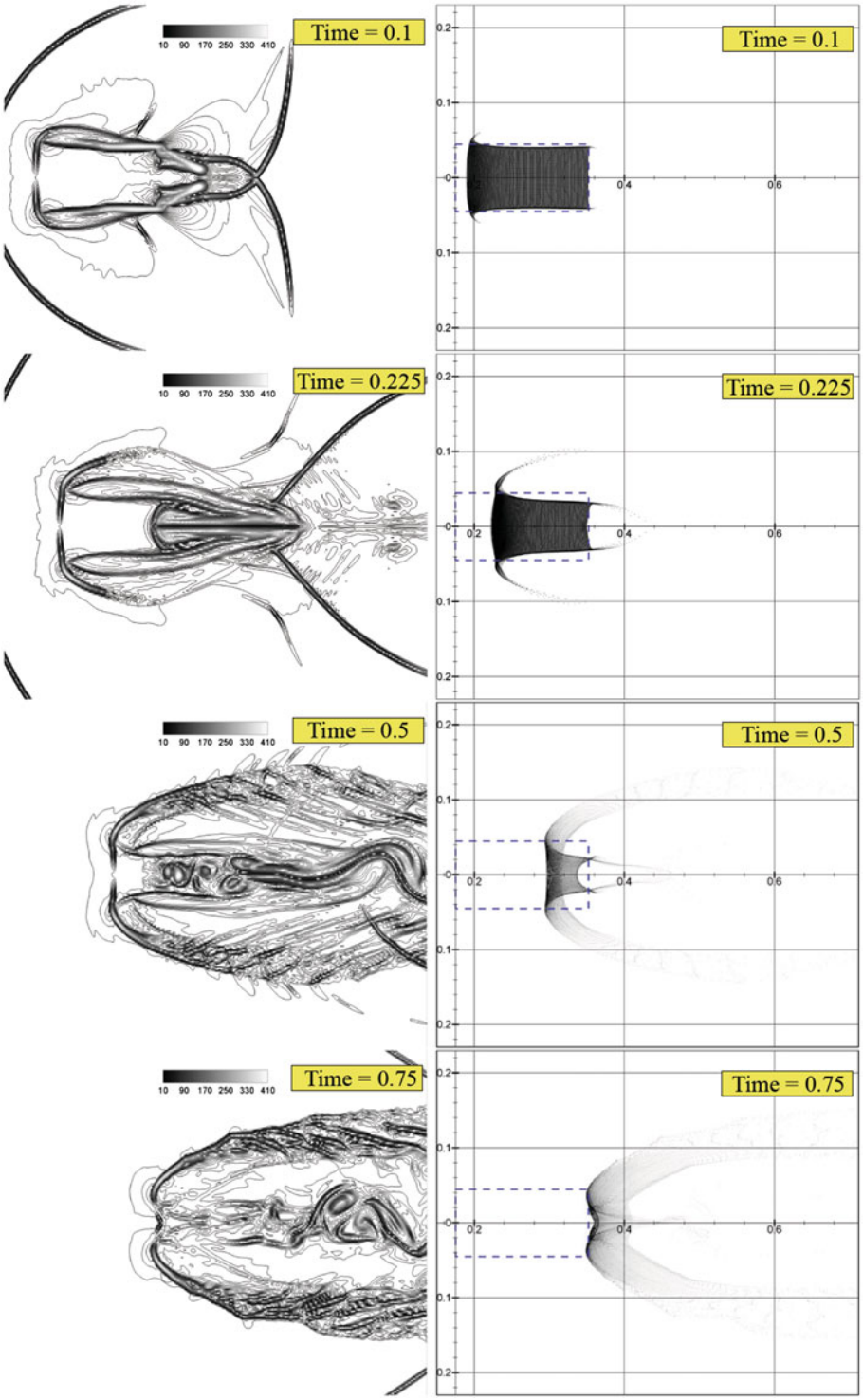

Fig. 2 A snapshot of the vorticity magnitude $|\omega|$ (*left column*) and the trajectory of the particle clouds (*right column*) for time $t = 0.1, 0.225, 0.5, 0.75$ (from *top* to *bottom*) as computed by the fifth-order WENO-Z/PSIC-5 method with ENO interpolation scheme. The *dotted rectangle* in the particle's trajectory figures shows the original shape and position of the rectangular particle cloud at $t = 0$ for easy reference. The shock Mach number is $M_s = 3$. The number of grid points used in the Eulerian frame is $1,500 \times 500$ in the x and y directions, respectively. The number of bronze particles in the rectangular cloud is 40 K

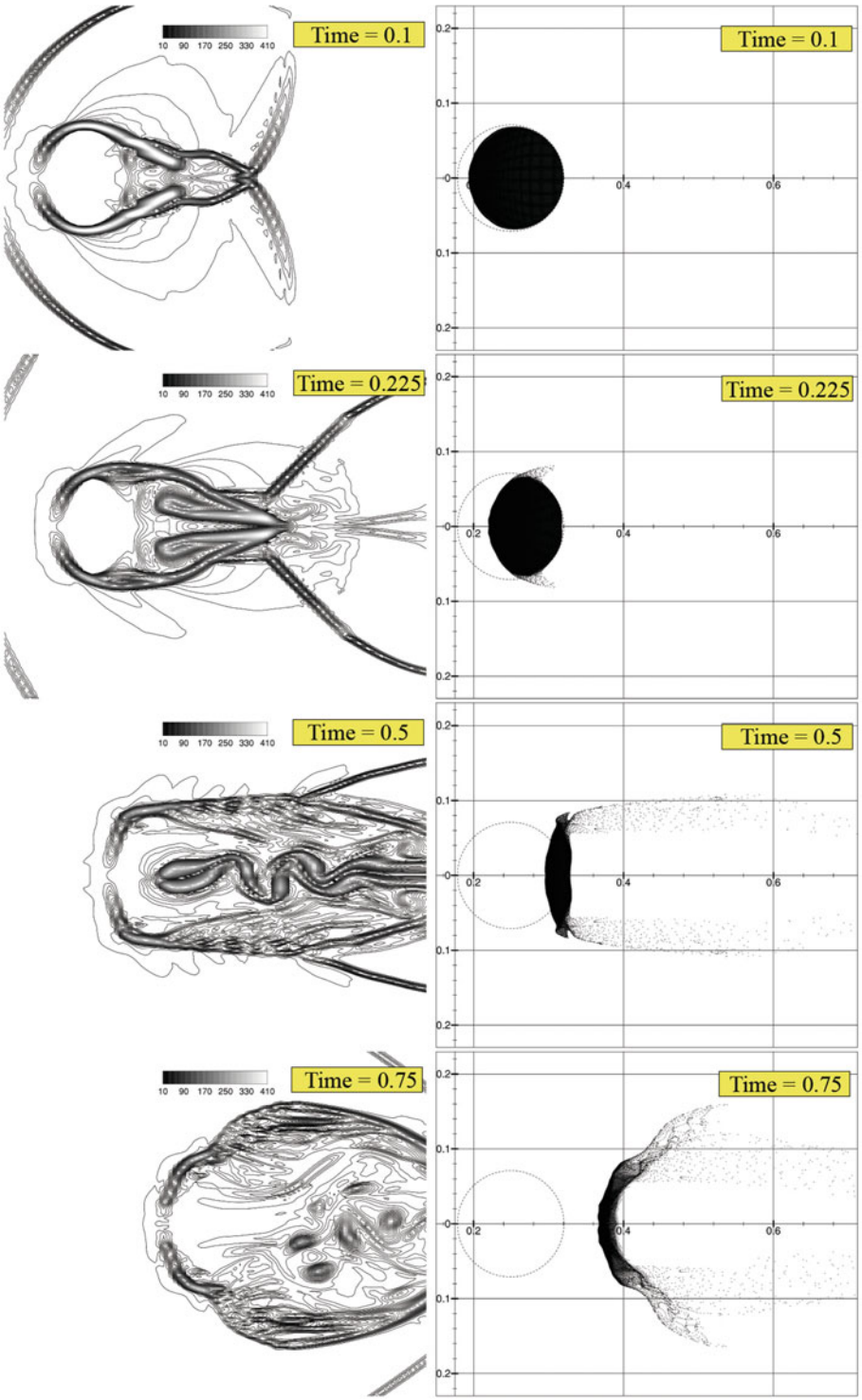

Fig. 3 A snapshot of the vorticity magnitude $|\omega|$ (*left column*) and the trajectory of the particle clouds (*right column*) for time $t = 0.1, 0.225, 0.5, 0.75$ (from *top* to *bottom*) as computed by the fifth-order WENO-Z/PSIC-5 method with ENO interpolation scheme. The *dotted triangle* in the particle's trajectory figures shows the original shape and position of the circular particle cloud at $t = 0$ for easy reference. The shock Mach number is $M_s = 3$. The number of grid points used in the Eulerian frame is $1,500 \times 500$ in the x and y directions, respectively. The number of bronze particles in the circular cloud is 40 K

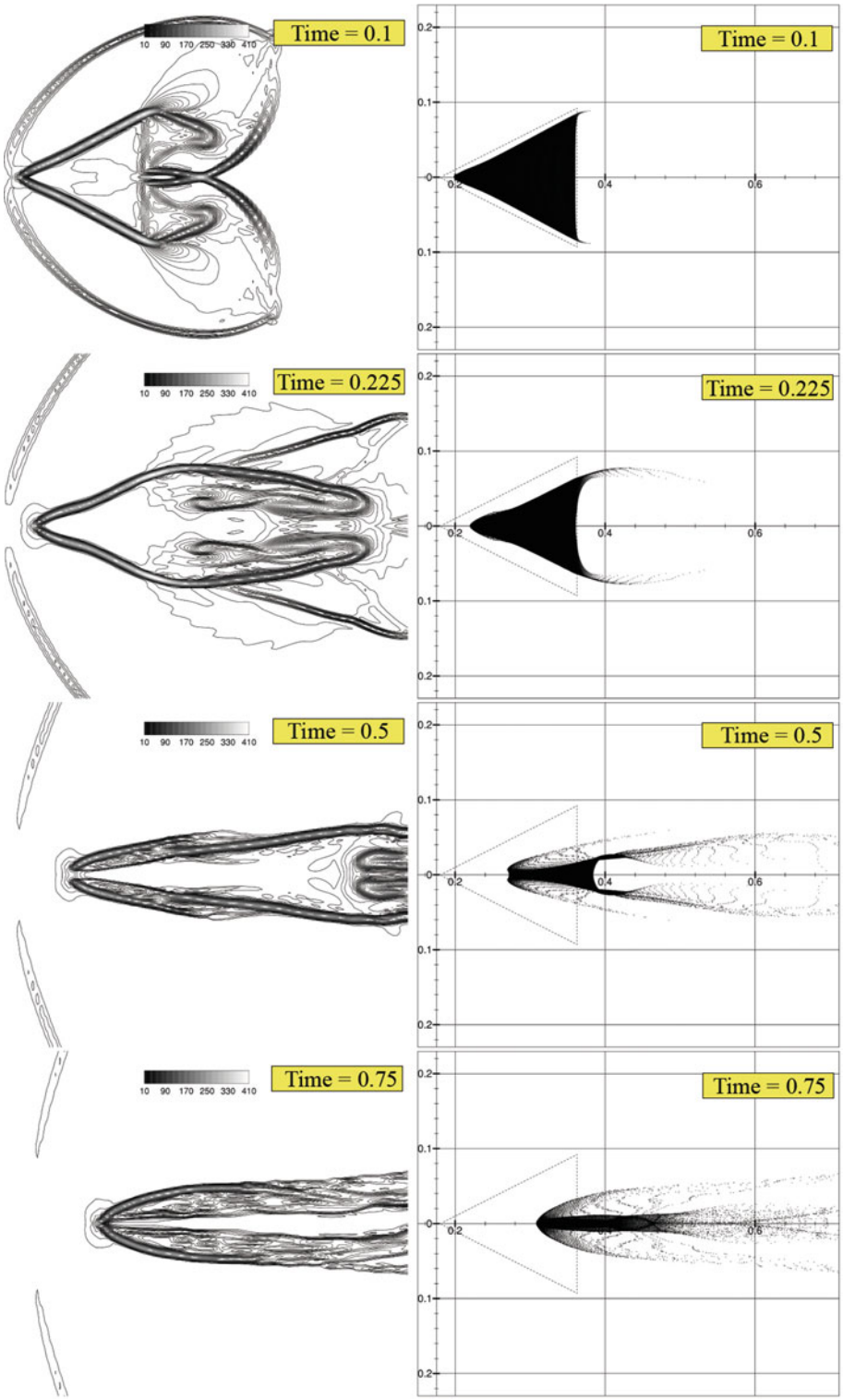

Fig. 4 A snapshot of the vorticity magnitude $|\omega|$ (*left column*) and the trajectory of the particle clouds (*right column*) for time $t = 0.1, 0.225, 0.5, 0.75$ (from *top* to *bottom*) as computed by the fifth order WENO-Z/PSIC-5 method with ENO interpolation scheme. The *dotted triangle* in the particle's trajectory shows the original shape and position of the triangular particle cloud at $t = 0$ for easy reference. The shock Mach number is $M_s = 3$. The number of grid points used in the Eulerian frame is 1,500 $\times$500 in the x and y directions, respectively. The number of bronze particles in the triangular cloud is 40 K

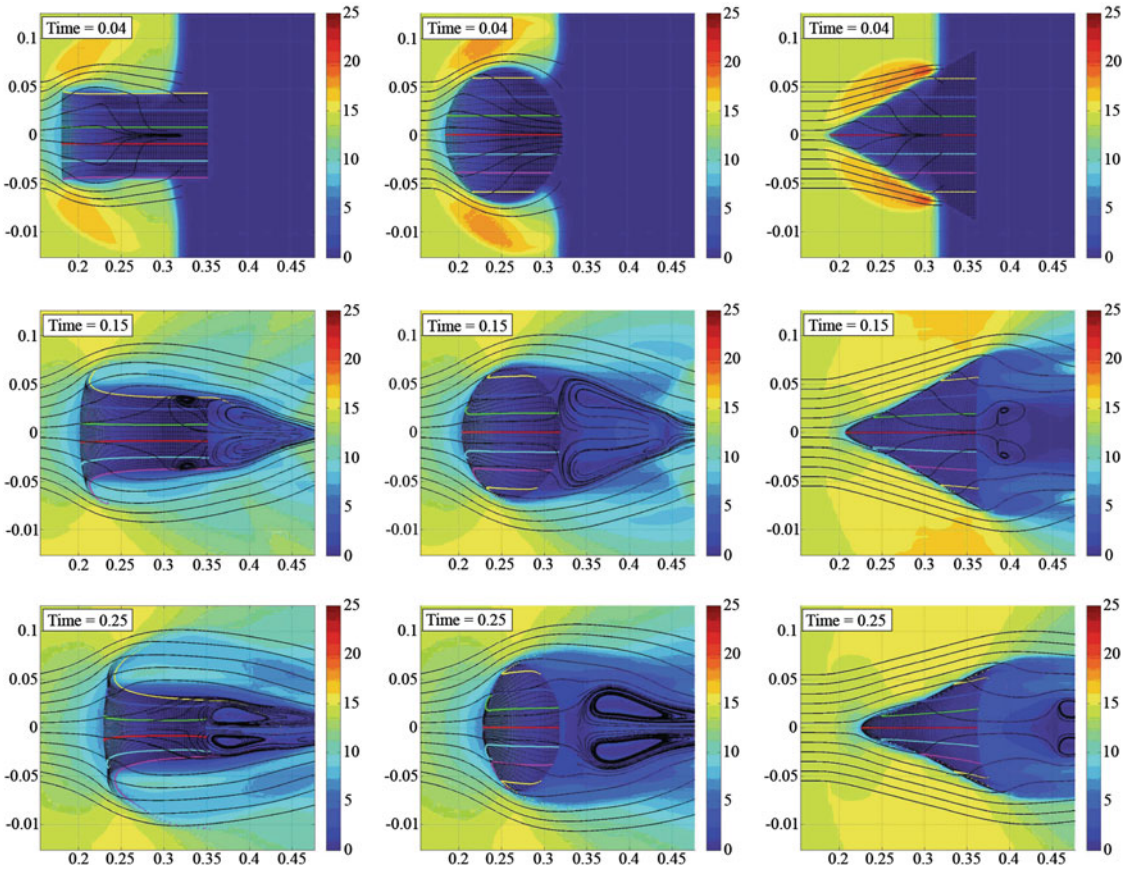

Fig. 5 A snapshot of the magnitude of the fluid velocity superimposed with the flow's streamlines, trajectories of the particles and colored particle streaks at early times, $t = 0.04$, 0.15 and 0.25 (top to bottom), for the (left) rectangular, (middle) triangular and (right) circular shaped particle clouds

Since the particle dynamics are greatly influence by the velocity magnitude and direction of the carrier fluid according to (6), we inspect the particle dynamics at early time in Fig. 5 against contours of the velocity magnitude and streamlines in the flow. We trace the development of initially horizontally oriented streak of particle identified by different coloring.

The fluid velocity is naturally lower inside the shape than outside. As a result, the particles that are located inside the cloud do not show significant motion at early time. The particles move mostly at the edges for all shapes. Whereas for the circular and triangular shape, the particles move along the front edges of the shape, the particles move away from the rectangular shape on the front and the rear corners. Particularly, the yellow and red streaks in the rectangular cloud shape show a significant deformation along the entire edge at $t = 0.15$. Since at the front end of the shape, the velocity magnitude and streamline deflection increase with increased distance from the symmetry, the particle streaks show a larger deformation away from the symmetry line.

At time $t = 0.15$, recirculation patterns have formed at the rear of the rectangular and circular particle clouds that compress the rear of the shape stream upwards, whereas for the triangular shape, there is no noticeable recirculation and compression.

At time $t = 0.25$, the increased carrier fluid velocity inside the cloud affects the particle streaks. The triangular shape flow shows streamlines that move into the shape inducing a compression of the streaks towards the symmetry line. The streamline and the streaks in the rectangular shape are deflected away from the symmetry line, whereas in the circular shape, the streamlines and streak are not showing significant deflection.

4.3 Particle-laden flow development at late time

The wake behind all shapes becomes unstable and loses its symmetry at later time (See Figures for $t = 0.5$ and $t = 0.75$). An asymmetric shedding is observed in the vorticity contour. Increasingly, more particles have dispersed out of the cloud, and the initial shape is hardly recognizable at later times.

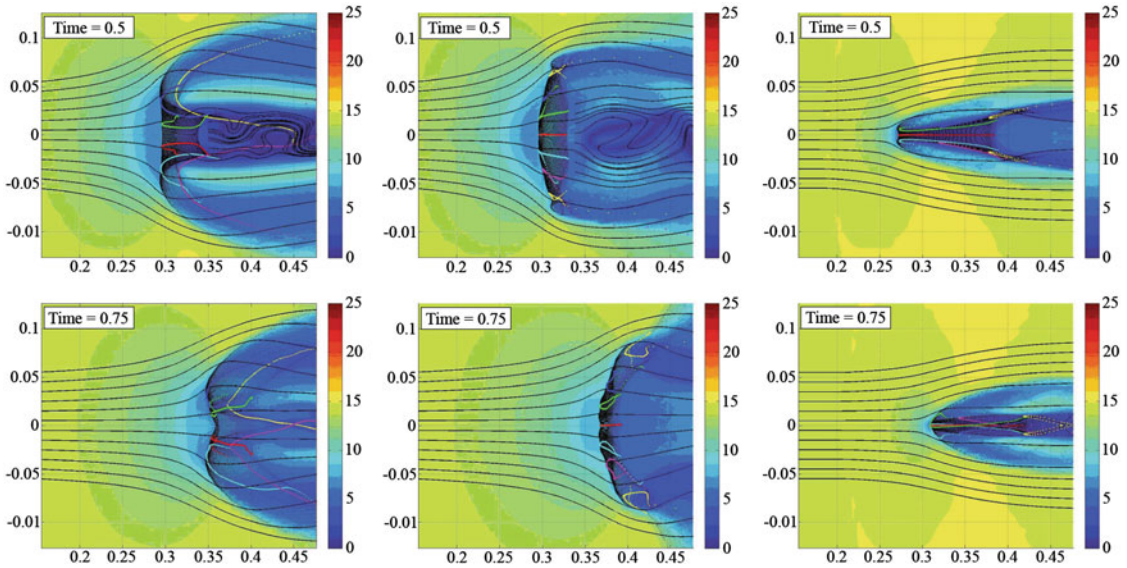

Fig. 6 A snapshot of the magnitude of the fluid velocity superimposed with the flow's streamlines, trajectories of the particles and colored particle streaks at late times, $t = 0.5$ and 0.75 (top to bottom), for the (left) rectangular, (middle) triangular and (right) circular shaped particle clouds

The particles have mostly compressed or have formed long and thicker particle streaks into the main flow originating from the initial shape.

For the rectangle case, most particles are transported in the arm that forms at the front corner of the rectangle. The flow separation at the front corners and hence the particle streak emanating from the front corners persist throughout the computed interval. The particle arm shields the wake flow from the rear of the rectangular shape. This results in low flow velocities at the rear stagnating the transport of particles into the legs at the rear at later times.

A separated shear layer also persists for the circle case at later times, yielding a continuous transport of particles in the particle streak. Initially, particles are drawn from the front half of the circle. Later on, the front half of the circle is compressed in streamwise direction, and flow that accelerates to the right encounters the wider rear half of the circle that was initially pushed upstream by the recirculation behind the circle. The rear half of the circle induces a new shear layer at time $t = 0.5$ that widens the influence of the particle cloud on the flow as seen through the larger cross-stream dispersion and wider wake at $t = 0.75$ when compared to $t = 0.5$. The particle-laden wake of the circle is approximately fifty percent wider than the rectangle particle-laden wake.

The wake from the triangular cloud shape is significantly narrower than the rectangular and circular cloud shapes. At later times, the front edge of the triangle has been compressed into a blunt nose. Two new particle streaks form off the front corners of this blunt following the separated shear layers in a comparable fashion to the case of the rectangular cloud shape. These new streaks reach further into the flow shielding the streaks at the rear end, which are further compressed toward the symmetry line.

With an increasing number of particles pulled out of the rectangular and circular shapes at late times, the particle concentrations reduce. As a result, the velocity magnitudes increased inside these shapes (Fig. 6), and the particles' velocity also increases. The streaks that were initially separated out of the rectangular cloud are now transported downstream, while maintaining their general shape.

The streaks in the triangular shape behave rather different when compared to the other two shapes. They continue to move towards the symmetry line at $t = 0.5$ and cross the symmetry line at $t = 0.75$. The streaks that stay straight form distinct diamond patterns at the rear end of the particle cloud at late times.

5 Conclusions and future developments

We have compared the computationally determined particle-laden flow developments of an initially rectangular, triangular and circular cloud of bronze particles in the accelerated flow behind a moving (detonation)

shock. The dispersion patterns and the dynamics of the particles from the three shapes are shown to be distinctly different, but there are similarities in the flow mechanisms.

At early times, particles are transported out of the initial shape following the separated shear flows from the shape. The flow separates trivially at the sharp corners of the rectangular and triangular shapes, leading to sharp particle streaks emanating from the clouds at these locations. The separation location is non-trivial and unsteady in case of the circular cloud shape and moves upstream at early times. Particles are transported into the flow from different locations of the shape at different times and hence form a particle streak that is less sharp.

The particle-laden wake is widest, and particles are dispersed most in cross-stream, for the initially circular cloud shape, while the particle-laden wake is narrowest for the triangular shape despite it being the widest shape initially. The primary reason for the narrow wake is that particles are only moving out of the shape towards the symmetry line following the separated shear layer at the *rear* of the triangle that curves inward toward the symmetry line. No separation occurs at the front of the triangle, since the reflected shock at the front of the triangular cloud is attached and weaker when compared to the shock reflected in the blunt circular and rectangular clouds. The flow also remains attached along the front edges of the triangle. The rectangle and circle both have a separated shear layers at the front of the shape that moves away from the center symmetry lines and hence widen the wake area. The particle-laden wake of the circular cloud is wider than the rectangular cloud, since a secondary separated shear layer away from the symmetry line is induced by the back half of the circle when the front half of the circle is compressed into the cloud by the accelerated flow.

We are currently characterizing the particle-laden flow developments for a large range of particle cloud shapes and particle materials in the accelerated flow behind moving shocks and will report on the complete characterization of the particle-laden flow developments when a shock hits a cloud of particles at rest in the near future. The purpose of this study is to generate a database for and a basic understanding of the basic features of flows that will enable the characterization of particle dispersion in dust explosion and the validation against complex experimental particle initializations. To model the physical problems of interest, a full Navier–Stokes solver is currently under development to take into account the viscous and thermal conductivity effects of the carrier fluids and we will report on the results of these simulations in future papers.

Acknowledgments The first author acknowledges the support of this work by AFOSR through a grant in the Young Investigator Program and by the University Grants Program at San Diego State University. The second author (Don) acknowledges the support of this research by the CERG grant of the Hong Kong Research Grant Council.

References

1. Abe, H., Natsuhiko, S., Itatani, R.: High-order spline interpolations in the particle simulation. J. Comp. Phys. **63**, 247–267 (1986)
2. Balsara, D., Shu, C.: Monotonicity preserving weighted essentially non-oscillatory schemes with increasingly high order of accuracy. J. Comp. Phys. **160**, 405–452 (2000)
3. Boiko, V., Kiselev, V., Kiselev, S., Papyrin, A., Poplavsky, S., Fomin, V.: Shock wave interaction with a cloud of particles. Shock Waves **7**, 275–285 (1997)
4. Borges, R., Carmona, M., Costa, B., Don, W.S.: An improved weighted essentially non-oscillatory scheme for hyperbolic conservation laws. J. Comp. Phys. **227**(6), 3191–3211 (2008)
5. Costa, B., Don, W.S., Gottlieb, D.: Two-dimensional multi-domain hybrid spectral-WENO methods for conservation laws. Comm. Comp. Phys. **1**(3), 548–574 (2006)
6. Crowe, C.T., Sharma, M.P., Stock, D.E.: The particle-source in cell (PSI-Cell) model for gas-droplet flows. J. Fluids Eng. **6**, 325–332 (1977)
7. Jacobs, G., Don, W.S.: A high-order WENO-Z finite difference based particle-source-in-cell method for computation of particle-laden flows with shocks. J. Comp. Phys. **228**(5), 1365–1379 (2008)
8. Jacobs, G.B., Hesthaven, J.S.: High-order nodal discontinuous Galerkin particle-in-cell method on unstructured grids. J. Comp. Phys. **214**, 96–121 (2006)
9. Jiang, G., Shu, C.: Efficient implementation of weighted eno schemes. J. Comp. Phys. **126**, 202–228 (1996)
10. Kiselev, V., Kiselev, S., Vorozhtsov, E.: Interaction of shock wave a particle cloud of finite size. Shock Waves **16**, 53–64 (2006)
11. Latini, M., Schilling, O., Don, W.S.: Effects of spatial resolution and order of WENO spatial reconstruction on mixing for two-dimensional Richtmyer-Meshkov instability with reshock. J. Comp. Phys. **221**, 805–836 (2007)
12. Latini, M., Schilling, O., Don, W.S.: High-resolution simulations and modeling of reshocked single-mode richtmyer-meshkov instability: comparison to experimental data and to amplitude growth model predictions. Phys. Fluids **19**, 024104, 1–19 (2007)
13. Roe, P.L.: Approximate Riemann solvers, parameter vectors, and difference schemes. J. Comp. Phys. **43**, 357–372 (1981)
14. Shu, C.W.: Essentially non-oscillatory and weighted essentially non-osillatory schemes for hyperbolic conservation laws. ICASE Report 97-65, NASA Langley Research Center, Hampton, VA (1997)